Nanoscale

PAPER

View Article Online
View Journal

Cite this: DOI: 10.1039/d3nr00477e

A natural indirect-to-direct band gap transition in artificially fabricated MoS_2 and $MoSe_2$ flowers†

Jun Zhou, ‡[a] Juan Cui, ‡[b] Shuo Du,[c] Zihan Zhao,[d] Jianfeng Guo,[e] Songyang Li,[e] Weifeng Zhang,[d] Nan Liu,[d] Xiaotian Li,[a] Qinghu Bai,[c] Yang Guo,[c] Shuo Mi,[e] Zhihai Cheng,[e] Lin He,[a] J. C. Nie,[a] Yu Yang *[b] and Ruifen Dou *[a]

Twisted bilayer (tB) transition metal dichalcogenide (TMD) structures formed from two pieces of a periodic pattern overlaid with a relative twist manifest novel electronic and optical properties and correlated electronic phenomena. Here, twisted flower-like MoS_2 and $MoSe_2$ bilayers were artificially fabricated by the chemical vapor deposition (CVD) method. Photoluminescence (PL) studies demonstrated that an energy band structural transition from the indirect gap to the direct gap happened in the region away from the flower center in tB MoS_2 ($MoSe_2$) flower patterns, accompanied by an enhanced PL intensity. The indirect-to-direct-gap transition in the tB-MoS_2 ($MoSe_2$) flower dominantly originated from a gradually enlarged interlayer spacing and thus, interlayer decoupling during the spiral growth of tB flower patterns. Meanwhile, the expanded interlayer spacing resulted in a decreased effective mass of the electrons. This means that the charged exciton (trion) population was reduced and the neutral exciton density was increased to obtain the upgraded PL intensity in the off-center region. Our experimental results were further evidenced by the density functional theory (DFT) calculations of the energy band structures and the effective masses of electrons and holes for the artificial tB-MoS_2 flower with different interlayer spacings. The single-layer behavior of tB flower-like homobilayers provided a viable route to finely manipulate the energy band gap and the corresponding exotic optical properties by locally tuning the stacked structures and to satisfy the real requirement in TMD-based optoelectronic devices.

Received 1st February 2023,
Accepted 27th March 2023

DOI: 10.1039/d3nr00477e

rsc.li/nanoscale

1. Introduction

In two-dimensional (2D) materials, interlayer coupling and interaction, determined by the number of layers and the stacking configuration, are crucially important to govern the crystal symmetry and the electron Coulomb interactions, resulting in novel quantum phenomena.[1–8] For example, the Mott insulating state and superconductivity have been observed in magic-angle twisted bilayer graphene.[4–8] More recently, bilayer transition metal dichalcogenides (TMDs) have been predicted to be another 2D system for exploring exotic physical properties dependent on interlayer coupling through modulating the interlayer distance and stacking order.[9–19] Energy band structure tunability is among the most important properties of bilayer 2D TMDs, which is related to the modification of their electronic and optical properties and the correlated electronic phenomena.[14–26] It is reported that the energy band structures of TMDs can be engineered through the internal interlayer stacking configurations with respect to the twist angle[14–17] and external stimuli such as strain,[18–23] temperature,[24] and plasma.[25–27] Theoretical work has demonstrated that bilayer TMDs with a special twist angle exhibit an ultra-flat band and might be an ideal system for investigating the correlated electronic states.[13] In addition, for bilayer and multilayer TMDs, a tunable energy band structure as well as an enhanced photoluminescence (PL) intensity can be accomplished through a twist angle and other stimuli.[18–26] It has been accepted that direct-gap bilayer TMDs greatly upgrade the optical densities compared to the monolayers while increasing the PL yield. This means that bilayer TMDs with a direct-gap feature can be potentially utilized in practical optoelectronic devices because they complement the small optical density deficiency of the

[a]Department of Physics, Beijing Normal University, Beijing, 100875, China. E-mail: rfdou@bnu.edu.cn
[b]LCP, Inst Appl Phys & Computation Math, Beijing 100088, China. E-mail: Yang_yu@iapcm.ac.cn
[c]Beijing National Laboratory for Condensed Matter Physics, Institute of Physics, Chinese Academy of Sciences, Beijing 100190, China
[d]Beijing Key Laboratory of Energy Conversion and Storage Materials, College of Chemistry, Beijing Normal University, 100875, China
[e]Department of Physics and Beijing Key Laboratory of Optoelectronic Functional Materials & Micro-nano Devices, Renmin University of China, Beijing 100872, P. R. China

†Electronic supplementary information (ESI) available. See DOI: https://doi.org/10.1039/d3nr00477e

‡These authors equally contributed to this work.

monolayers. Therefore, the controllable fabrication of direct-gap-like bilayer TMDs is extremely necessary to understand the physics underlined in the indirect-to-direct-gap transition and is also a feasible approach for realizing the application of bilayer TMDs in real optoelectronic devices.

As we have mentioned above, some efforts have been devoted to developing approaches for preparing direct-gap-like bilayer and multilayer TMDs.[18–28] Among the most feasible methods is the modification of the TMDs' interlayer spacing and thus tuning of the band structures through the O_2 plasma treatment of the bulk TMDs.[25–27] However, some uncontrollable defects, such as various vacancies and antisite defects of transition metals and chalcogens in 2D TMD systems, can be generated during the post-treatment process, which would locally change their optical properties and bring out some application uncertainties.[27–29] To date, there have been few reports on tuning the switching of the energy band structures of bilayer TMDs from the indirect gap to the direct one through manipulating the interlayer stacking order. Besides, it is necessary to theoretically and deeply understand the nature of the energy band structural evolution influenced by the stacked structures dependent on the twist, the interlayer distance, *etc*. Accordingly, an easy and one-step synthesis method of TMD materials tuned by the interlayer twist and special interlayer configuration, exhibiting a direct-gap-like behavior, is very desirable from both the fundamental and applied research points of view.

In this contribution, we demonstrate a series of twisted bilayer (tB) MoS_2 patterns with a three-fold symmetric flower-like shape and versatile twist angles (about 16°, 21°, 25°, 30°, 36°, and 45°) that were artificially fabricated by the chemical vapor deposition (CVD) method. We found that the artificial tB-MoS_2 flowers exhibit strong direct bandgap-like PL emission and intense monolayer-like optical properties in the region away from the flower center. In contrast, MoS_2 flower patterns with a twist angle of 0° or 60° could retain an indirect gap feature and a weakened PL intensity. A similar direct bandgap-like behavior could be reproduced in the tB-$MoSe_2$ flower with a twist angle of approximately 56°. The origin of the indirect-to-direct bandgap transition with an enhanced PL intensity in the tB-MoS_2 and $MoSe_2$ flowers was rationally elucidated by combined measurements, including Raman spectroscopy, PL spectroscopy, atomic force microscopy (AFM), UV-vis adsorption spectroscopy and the density functional theory (DFT) calculations of the energy band structure and the effective masses of electrons and the holes. The Raman spectra and PL results displayed an expanded spacing in the off-center regions for all twisted flower patterns. Meanwhile, AFM and UV-vis adsorption spectral measurements evidenced a gradually expanded interlayer spacing from the flower center to the off-center region in the non-zero tB-MoS_2 flower patterns compared to those of 0° (60°)-tB-MoS_2 flower patterns. These were probably generated by the spiral growth of the second flower-like MoS_2 ($MoSe_2$) layer with a twist related to the first layer. The enlarged interlayer distance resulted in interlayer decoupling and a decline of the effective masses of electrons and holes. The former directly led to the indirect-to-direct-gap transition, while the latter facilitated the reduction in charged exciton (trion) density and thus, the PL intensity enhancement in the twisted MoS_2 ($MoSe_2$) flower patterns. The above experimental results could be efficiently elucidated by DFT calculations of the energy band structures and effective masses of the electrons and the holes of tB-MoS_2 flowers tuned by different interlayer spacings. The enhanced PL intensity and single-layer behaviors of twisted MoS_2 and $MoSe_2$ flower patterns demonstrated a potential avenue of tuning twisted bilayer TMD materials by generating the interlayer twist and locally changeable interlayer distances to satisfy their high performance in optoelectronics.

2. Results and discussion

Stacked bilayer MoS_2 flakes with rich twisted angles and a flower-like pattern were prepared on the SiO_2/Si substrate using a feasible CVD approach. In our work, the SiO_2/Si substrate was face-down placed on a quartz boat at an obliquel angle relative to the carrier gas flow, which may cause a step change in the substrate temperature and the gas flow rate. Under this circumstance, the translation and rotation have different consequences during the nucleation and growth of MoS_2, which is referred to as a growth mode of screw-dislocated spirals of 2D materials on non-Euclidean surfaces.[30] This growth process is consistent with previously reported growth parameters during the CVD growth process.[30] Therefore, bilayer MoS_2 nanostructures with a twist and continuously expanded spacings could be generated. Meanwhile, in the present case, the Mo concentration is controlled to be low, so as to ensure the fractal growth of the thin film, which is discussed in detail in the former work.[30] As a result, AA and AB stacking configurations, the most stable bilayer structures with the lowest formation energy can be broken using the above growth parameters,[31] and twisted bilayer MoS_2 patterns with a flower shape form due to the screw-dislocated spiral growth coexisting with the fractal growth of bilayer MoS_2. The universal growth procedure is described in the Methods section, and the detailed growth mechanism of the tB-MoS_2 flower patterns will be discussed elsewhere.[32] More interestingly, a series of tB-MoS_2 flower patterns with diverse interlayer twists of approximately 0°, 16°, 21°, 25°, 30°, 36°, 45°, and 60° were obtained. The typical optical microscopy (OM) images of the tB-MoS_2 flower with twist angles of 21° and 0° are respectively shown in Fig. 1a and b. More optical microscope images of tB-MoS_2 with versatile interlayer twists can be seen in Fig. S1 in the ESI.† The contours of the flower shape and triangular shape for the top and bottom layer in the bilayer MoS_2 pattern are outlined by black lines in Fig. 1a and b. The interlayer twist (θ) of the bilayer MoS_2 structure is ascertained by comparing the rotation angle of the symmetric axis of the top flower pattern related to that of the bottom triangular shape, which is displayed by a twist (θ) of the white and black dashed lines in Fig. 1a. AFM measurements were comparably per-

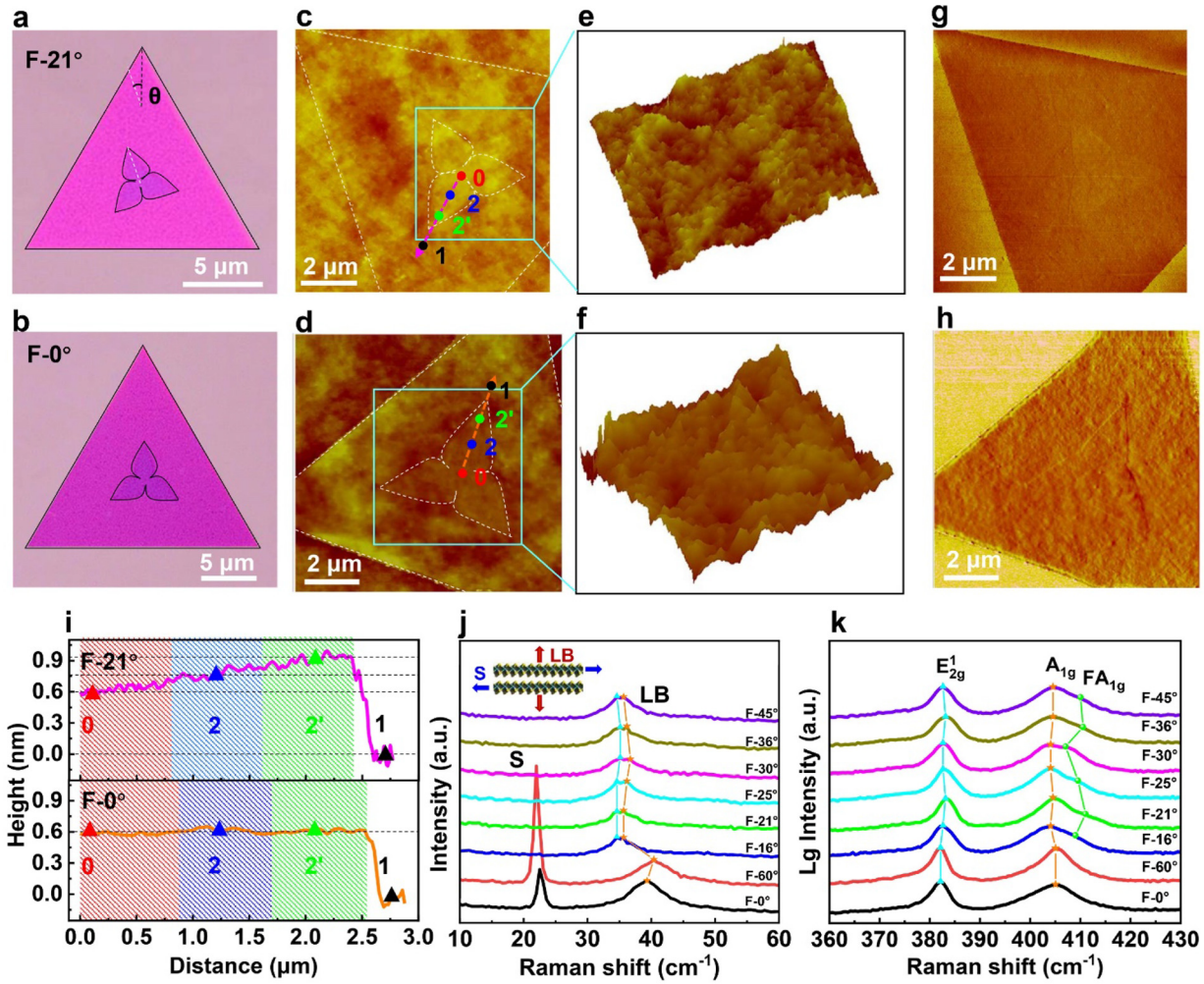

Fig. 1 Atomic force microscopy images, and low-frequency and high-frequency Raman spectra of tB-MoS_2 flowers. (a and b) OM images of the tB-MoS_2 flower patterns with a twist of approximately 21° (a) and 0° (b), respectively. The twist-angle is enclosed in the left upper numbers in (a) and (b), respectively. (c and d) AFM topographic images of the tB-MoS_2 flower pattern at θ = 21° and 0°, respectively. (e and f) The top flower patterns are zoomed in on the right parts of (c) and (d) to display the topographic and height difference in tB-MoS_2 flower patterns with different twists. (g and h) AFM phase images corresponding to (c) and (d) of the tB-MoS_2 flower pattern at θ = 21° and 0°, respectively. (i) A height profile in (c) and (d) marked with pink and orange, showing the changeable interlayer spacing from the center to the off-center region for the 21°-tB-MoS_2 flower. (j and k) LF and HF Raman spectra obtained from the tB-MoS_2 flower patterns with twist angles of about 0°, 16°, 21°, 25°, 30°, 36°, 45°, and 60°. The schematic model of the atomic vibration modes of S and LB is shown in the upper inset of Fig. 1j.

formed on tB-MoS_2 flower-like patterns to confirm the thickness and evaluate the interlayer spacing between the top and bottom layers. Fig. 1c and d show typical AFM topographic images of the 21°- and 0°-tB-MoS_2 flower patterns, respectively. The flower contour of the top layer could be obviously discerned, as shown in zoomed AFM images in Fig. 1e and f and two AFM phase images (Fig. 1g and 1h) corresponding to Fig. 1c and d, respectively. A profile line from the top to the bottom layer in Fig. 1c and d are respectively marked by pink and orange arrows for a clear identification of the interlayer spacing. In Fig. 1i, the pink profile line from the top layer in the 21°-tB-MoS_2 flower pattern shows that the interlayer spacing between the upper and the lower layer varied from 0.63 to 0.75 nm, and to 0.95 nm, corresponding to the center region (**0**), to region (**2**) and the off-center region (2′) in the 21°-tB-MoS_2 flower. In contrast with the AFM image of the 0°-tB-MoS_2 flower, the interlayer spacing was constantly detected as about 0.60 nm from the whole flower pattern, as shown by the orange line in Fig. 1i. To evidence the interlayer distance depending on the tB-MoS_2 flower patterns with different twists, the AFM topographic and phase images of the 30°-tB-MoS_2 flower pattern are provided in Fig. S2.† We can clearly see that the interlayer spacing between the top and the bottom layer is a constant value from the profile line (Fig. S2†). The gradually enlarged interlayer spacing[33] may induce interlayer decoupling that is thus unambiguous to affect the energy band structure and optical properties of the bilayer TMD system, which will be discussed in the following section.

The thickness and interlayer coupling can also be probed by measuring low- and high-frequency Raman vibration spec-

troscopy. As previously reported, bilayer TMD materials possess a set of shear (S) modes and layer-breathing (LB) modes which involve lateral and vertical displacement of individual layers, respectively.[34–40] These interlayer phonon modes are highly dependent on interfacial conditions and interlayer coupling, and can be tuned by the interlayer twisting and spacing. Moreover, the low-frequency (LF) Raman spectra are more sensitive to the details of the interface than the high-frequency (HF) Raman vibration modes.[9,10,35–41] Herein, we systematically investigated the characteristics of LF Raman spectra of the tB-MoS_2 flower patterns with interlayer twists of about 0°, 16°, 21°, 25°, 30°, 36°, 45°, and 60°. LF Raman spectroscopy was measured in different positions of the as-prepared samples to consider the interlayer distance effect, as shown in the upper part of Fig. S3b–i.† Obviously, Raman spectra from different detected locations in the tB-MoS_2 bilayer with a fixed twist exhibited similar features for the as-prepared tB-MoS_2 flower patterns in our experiments. The detailed analysis of the LF Raman spectra from different samples is provided in the ESI.† Interestingly, we observed an LB mode splitting into two modes in the tB-MoS_2 bilayer flower patterns with interlayer twists from 16°, 21°, 25°, 30°, and 36° to 45°, as shown in Fig. 1j and Fig. S3c–h.† This is probably due to the nonuniform interface caused by the strain generated by the spiral growth of twisted flower patterns, in agreement with the former studies.[41–45] However, for the tB-MoS_2 flower without a twist ($\theta = 0°$), except for an S mode at around 22.51 cm^{-1} and an LB mode at 39.36 cm^{-1} in the LF Raman spectroscopy, the split LB modes vanished, as shown in Fig. 1k and Fig. S3b,† very similar to the case of the 60°-tB-MoS_2 flower (Fig. S3i†). In a word, the above results revealed that interlayer twists affected the interfacial conditions and interlayer coupling at the tB-MoS_2 flower system. Accordingly, we can see that the different stacked structures induced by interlayer twists play an important role in the LF Raman results.

Besides, the different stacked structures could manipulate the HF Raman spectroscopy. Fig. 1k shows the HF Raman spectra from different twist-angle MoS_2 bilayer flower patterns. (HF Raman spectroscopy from different positions of the as-prepared samples, as shown in the lower part of Fig. S3b–i.†) Two prominent peaks located at around 383.16 cm^{-1} and 404.09 cm^{-1} were observed in the Raman curves of the as-prepared twisted MoS_2 bilayer samples (except for 0° (60°)-tB-MoS_2), respectively, corresponding to the in-plane E^1_{2g} mode and the out-of-plane A_{1g} mode. Thus, the frequency difference was about 22 cm^{-1} which is well consistent with the value of the typical bilayer MoS_2 on SiO_2/Si.[9–12] Meanwhile, compared with the peak of the mode of 0° (60°)-tB MoS_2, the detected E^1_{2g} peak underwent a blue-shift in HF Raman curves for non-zero tB-MoS_2 flower patterns, as shown in Fig. 1k. This is similar to the case of the LB mode splitting in LF Raman curves, probably resulting from the in-plain strain breaking the hexagonal symmetry.[42–48] Additionally, the moiré phonon mode (410.55 cm^{-1}), related to the A_{1g} phonon branch (FA_{1g}), is visible in HF Raman curves for 16°-, 21°-, 25°-, 30°-, 36°-, and 45°-tB MoS_2 flower patterns in Fig. 1k and the lower part of Fig. S3c–h,† originating from the off-center phonons of the monolayer linked with the lattice vectors of moiré reciprocal space.[9,11] In contrast, for the tB-MoS_2 flower with twists of 0° and 60°, the moiré phonon mode cannot be measured in the HF Raman spectra (the red and the black curve in Fig. 1k and the lower part of Fig. S3b and i†). These results are consistent with the former investigations on the moiré phonon detected in the moiré superlattice structures.[9–12,16] Accordingly, we found that bilayer flower patterns are tuned not only by twist angles but also by interlayer spacing, which could induce the energy band structures and optical properties to be unusual compared to the same structure but without an interlayer twist.

Comparably PL measurements were performed on the above samples. Typical PL spectra obtained at different positions indicated by four colored dots (the inset of Fig. 2a) of the sample of the 21°-tB-MoS_2 flower pattern are shown in Fig. 2a. It is obvious that the maximum PL intensity varied along different locations. Firstly, the black PL spectrum from region **1** showed a direct band gap character with a strong peak A with the exciton protrusion at 1.824 eV and a weak peak B with the exciton energy of 1.948 eV, consistent with the PL spectroscopy of monolayer MoS_2. Secondly, the red curve from the center of the flower-like bilayer (region **0**) showed that the intensity of the A exciton intensively dropped down, and a low energy peak appeared at 1.548 eV, suggesting an indirect gap feature similar to the case of the 21°-tB-MoS_2 bilayer. However, the PL intensity of the blue curve from region **2** increased with an indirect gap peak. Very interestingly, the PL intensity of the green curve from region **2′** dramatically enhanced up to a value similar to the monolayer MoS_2 and the indirect gap completely disappeared. These PL results could be reproduced in other samples of 16°-, 25°-, 30°-, 36°-, and 45°-tB-MoS_2 artificially stacked flowers, as shown in Fig. S4a_i–e_i.† From the PL intensity mapping images of the 21°-tB-MoS_2 flower detected at the indirect gap value (1.548 eV) and A exciton energy value (1.817 eV, Fig. 5Sa of the ESI), shown in Fig. 2c, we can clearly see that the area of the flower shape was reduced due to the increased PL intensity and disappearance in the indirect gap in the off-center region. This strongly suggests that from the center region to the off-center region, the energy band structure gradually changed from the indirect gap to the directgap in the 21°-tB-MoS_2 flower pattern. However, the PL spectra from the whole second layer of the sample of the 0°-tB-MoS_2 flower in Fig. 2b show a standard PL trait of the bilayer MoS_2, analogous to samples of the 60°-tB-MoS_2 flower pattern as shown in Fig. S4f_i.† Moreover, the PL intensity mapping images at the indirect gap (1.386 eV) in Fig. 2d and the direct gap (1.802 eV, Fig. S5b of the ESI) show a complete flower-like shape, illustrating that the intensity of the whole bilayer area was homogeneous and the indirect energy gap was retained. This means that the indirect-to-direct-gap transition merely happened in tB-MoS_2 flower patterns with a non-zero interlayer twist. Meanwhile, the starkly increased PL intensities in region **2′** from samples of 16°-, 21°-, 25°-, 30°-, 36°-, and 45°-tB-MoS_2

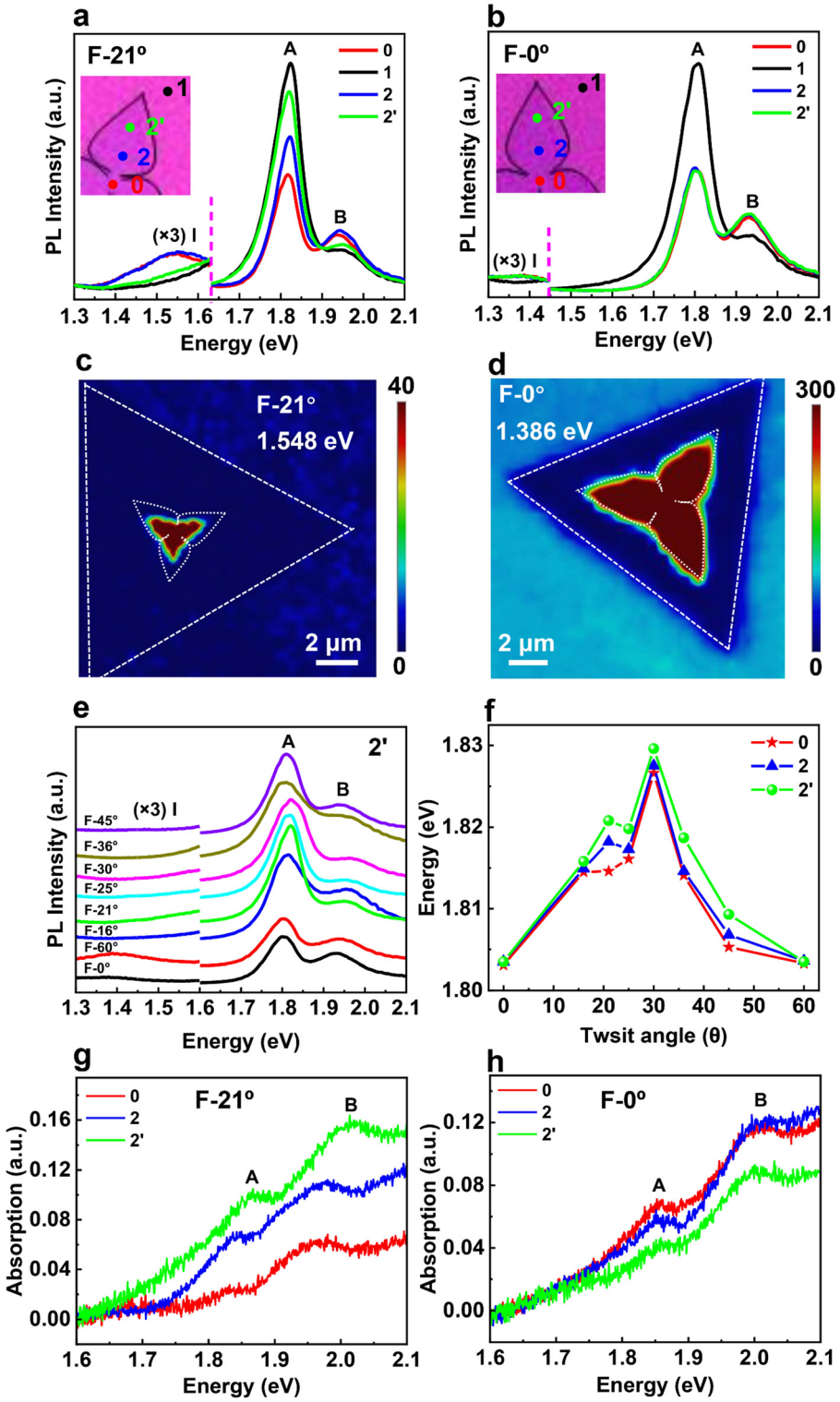

Fig. 2 PL spectroscopy measurements of the tB-MoS_2 flowers. (a and b) PL spectra acquired at different regions of the tB-MoS_2 flower patterns at θ = 21° and θ = 0°, the different colored curves corresponding to the colored dots in the OM image of the upper-left inset, respectively. (c and d) PL intensity mapping images of the 21°-tB-MoS_2 and 0°-tB-MoS_2 flower patterns obtained at the energy of I exciton peak positions of 1.548 and 1.386 eV, respectively. (e) The spectra from samples of 0°-, 16°-, 21°-, 25°-,30°-, 36°-, 45°-, and 60°-tB-MoS_2 flower patterns. (f) The energy position of the A exciton obtained in different regions (**0**, **2**, and **2'**) in the Tb-MoS_2 flower pattern with various twists. (g and h) The adsorption spectra of the samples of 21°-tB-MoS_2 and 0°-tB-MoS_2, respectively.

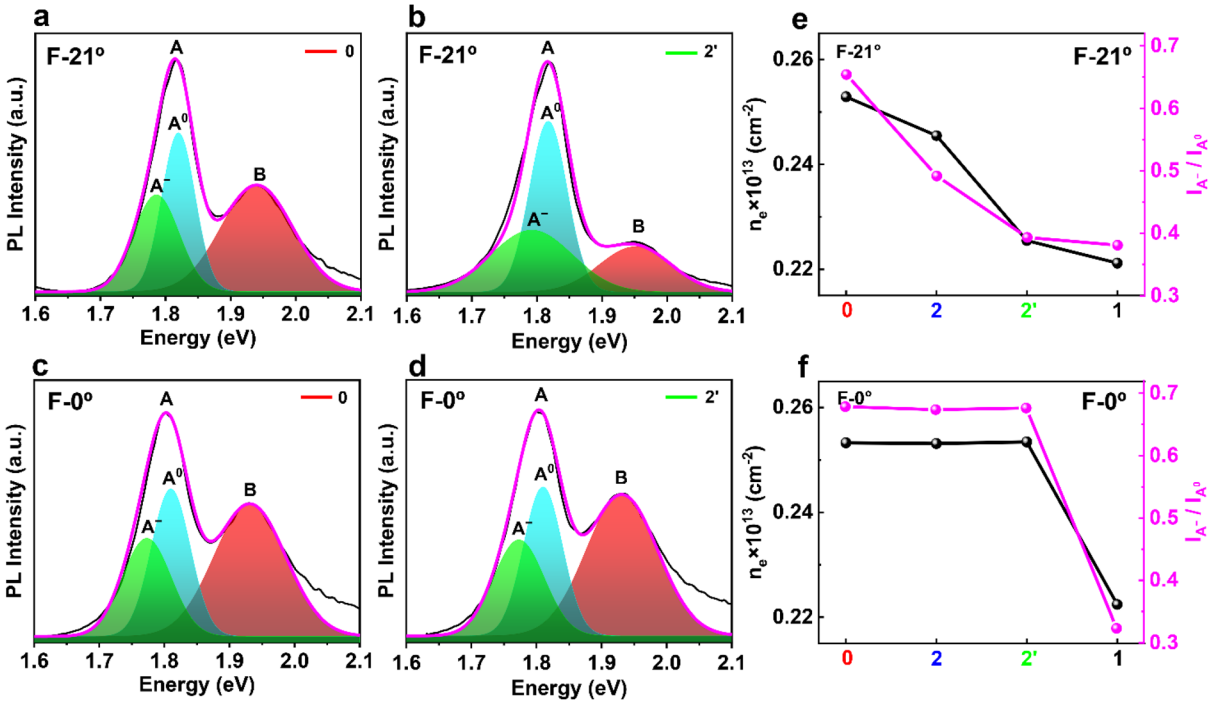

Fig. 3 (a and b) PL spectra obtained in regions **0** and **2′** of the 21°-tB-MoS_2 flower pattern with Gaussian fitting (PL components: A^- trion, A^0 exciton, and B exciton), respectively. (c and d) PL spectra obtained in regions **0** and **2′** of the 0°-tB-MoS_2 flower pattern with Gaussian fitting (PL components: A^- trion, A^0 exciton, and B exciton), respectively. (e and f) The relationship between the calculated electron charge concentration (n_e) and the ratio (R) of the negative trion weight (the green area) to the neutral exciton weight in different regions of **0**, **2**, and **2′** (the bilayer area) and region **1** (the monolayer area).

flowers were common, compared to 0°(60°)-tB-MoS_2 flower patterns, as shown in Fig. 2e. In addition, the energy of the A exciton obtained at region **0**, to **2** and **2′** correspondingly increased from 1.815 to 1.818 eV, and to 1.821 eV for samples of 16°-, 21°-, 25°-, 30°-, 36°-, and 45°-tB-MoS_2 flowers (Fig. 2f). This result was confirmed by the visible light adsorption spectra obtained at different regions of 21°-tB-MoS_2 as shown in Fig. 2g. This further evidences that the strained flower patterns with an expended interlayer distance in region **2′** exhibited an expanded energy gap, as reported in the former studies.[18,22,49–53] The adsorption spectra in the 0°-tB-MoS_2 flower pattern are shown in Fig. 2h, where the energy positions of the A exciton at different regions remained unchanged.

It is well-known that the direct electronic structure transition in TMDs originates from excitonic radiative relaxation.[54] We first considered the contributions of the neutral exciton (A^0) and the trion (A^-) in the PL peak A to understand the increased PL intensity and the indirect-to-direct band gap transition in the off-center region in the non-zero tB-MoS_2 flower pattern. Fig. 3a and b show the peak position and the PL intensity of the neutral exciton (A^0, blue line) and the negative trion (A^-, green line), respectively, corresponding to regions **0** and **2′** of the sample of the 21°-tB-MoS_2 flower pattern. This can be obtained by fitting the PL spectrum based on the Gaussian function deconvolution. Here, the ratio of the negative trion intensity (the green area) to the neutral exciton intensity (the shallow blue area) in the fitting PL curves in regions **0** and region **2** is defined as $R = I_{trion}/I_{exciton}$. Comparing $R_{2'}$ (~0.39) with R_0 (~0.65) in Fig. 3e, we conclude that the trion weight in region **2′** was intensively shrunk. A similar phenomenon was reproducible in other samples of 16°-, 25°-, 30°-, 36°-, and 45°-tB-MoS_2 flower patterns, as summarized in Fig. S4a_{ii}–f_{ii}.† However, from fitting the PL curve from region **0** to **2′** for the 0°-tB-MoS_2 flower pattern, respectively, as shown in Fig. 3c and d, one can see that there is a very close analogy between $R_{2'}$ and R_0, even though both values (~0.68) in Fig. 3f anf Fig. S6 of the ESI are from the different regions. This means that the trion concentration in the off-center region was lower than that in the center area in nonzero-twisted bilayer flower-like patterns (shown in the right ordinate in Fig. 3e), which generally facilitates the PL intensity enhancement. Correspondingly, the electron charge concentration (n_e), in different regions should be changeable, which is accordingly determined based on the former studies on the mass action law and is actually related to the ratio of I_{A^-} and I_{A^0}.[33,53] According to the mass action law, the ratio of the intensity A^- and A^0 can be expressed as

$$\frac{I_{A^-}}{I_{A^0}} = \frac{{}^{A^-}N_{A^-}}{{}^{A^0}N_{A^0}} = \frac{{}^{A^-}}{{}^{A^0}}\frac{\pi h^2 n_e M_{A^-}}{16 M_{A^0} m_e k_B T}\exp\left(\frac{\varepsilon_{A^-}}{k_B T}\right) \quad (1)$$

where, N_{A^-} abd N_{A^0} are the trion and exciton concentrations, respectively; Γ_{A^-} and Γ_{A^0} represent the radiative recombination rates of the trion and exciton, respectively; n_e, ε_{A^-}, and m_e are

excess electron concentration, trion binding energy, and electron effective mass at the K point of the Brillouin zone, respectively; M_{A^-}, M_{A^0} are the effective masses of the trion and the exciton, respectively.

Assuming that Γ_{A^-} and Γ_{A^0} are insensitive to the twisted angle,[33] the electron charge concentration can finally be expressed as

$$n_e = \frac{I_{A^-}}{I_{A^0}} \frac{16\pi M_{A^0} m_e k_B T}{h^2 M_{A^-}} \exp\left(\frac{\varepsilon_{A^-}}{k_B T}\right) \quad (2)$$

Here, m_e and m_0 are the electron and hole effective masses at the K point of the Brillouin zone that can be calculated using the first-principles theory after considering the various interlayer spacings. The detailed calculation process of our work is provided in Table S1 of the ESI.† M_{A^-} and M_{A^0} of the effective masses of the trion and the exciton can be accordingly obtained. I_{A^-}/I_{A^0} was determined by the PL spectra obtained in two typical samples of 21°- and 0°-tB-MoS_2. The electron charge concentrations (n_e) in different regions **0**, **2**, and **2′** from the MoS_2 bilayer and region **1** from the monolayer are shown in Fig. 3e and f, respectively, corresponding to the samples 21°-tB-MoS_2 and 0°-tB-MoS_2. It clearly shows a decreased electron concentration from the bilayer region **0** (0.425×10^{13} cm^{-1}) to region **2′** (0.22×10^{13} cm^{-1}) in the 21°-tB-MoS_2 flower pattern. This may be originated from the electron localization in the center of the flower pattern induced by the enlarged interlayer spacing, suppressing charge transfer from the bottom layer to the top layer near the off-center region. Therefore, the charged trion concentration was reduced and the PL intensity was enormously increased in the off-center region. As for the origin of the indirect-to-direct

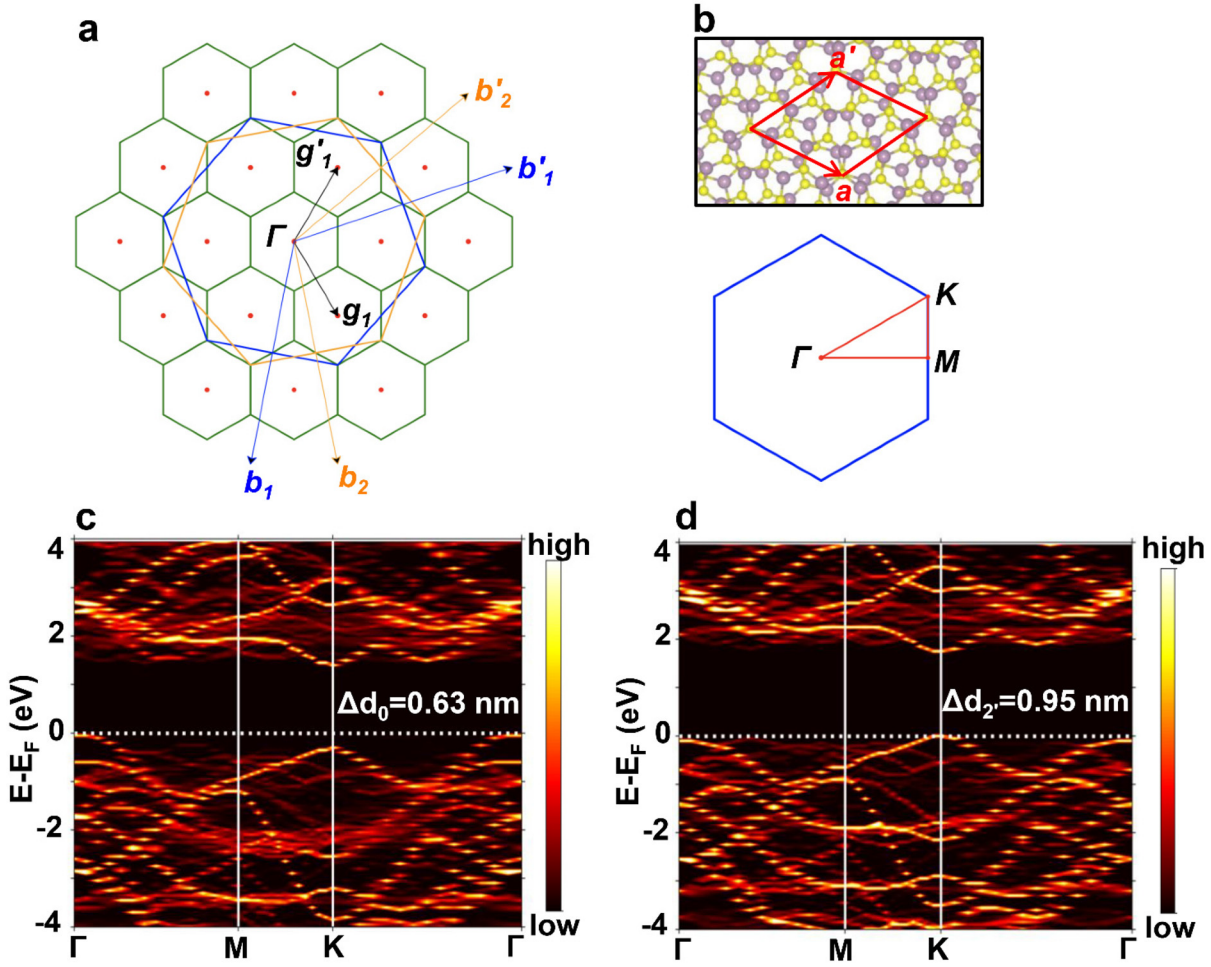

Fig. 4 DFT calculations of the energy band structures of tB-MoS_2 with various interlayer spacings. (a) The reciprocal lattice of the twisted bilayer MoS_2 with θ = 21.79°. The large blue and orange hexagons are the first BZ of the top and bottom MoS_2 layers, and the solid green hexagons represent the Wigner–Seitz cells of the reciprocal lattices of the crystallographic superlattices. (b) View of the atomic structure of twisted bilayer MoS_2 along the out-of-plane direction and the schematic diagram of the first BZ and the corresponding high-symmetry points. The red parallelogram represents the crystallographic superlattice unit cell of the structure. Note that the moiré pattern shows the same unit cell with the crystallographic superlattices in this structure. (c and d) Effective energy band structure of tB-MoS_2 at the center region **0** with the interlayer distance $\Delta d_0 = d_0 - d_1$ = 0.63 nm and at the edge region **2′** with $\Delta d_{2'} = d_{2'} - d_1$ = 0.95 nm under the strain field. The changed interlayer distance is also shown in Fig. S7.†

band gap transition near the off-center region in the artificial MoS_2 flowers, the changeable interlayer spacing plays the key role that should be considered to calculate the energy band structure of tB-MoS_2 in the K space.

We performed DFT calculations of the energy band structures for different regions of the tB-MoS_2 flower pattern to confirm the above speculations. Due to the spiral growth of the tB-MoS_2 flower pattern, the interlayer spacings were variant from the center region **0** and the off-center region **2′**. We simulated the twisted bilayer MoS_2 superlattice at different regions with a twisting angle of 21.79° and different interlayer spacings following the experimental data. Calculation details can be found in Fig. S7 and the ESI.† The reciprocal and real lattice structures of twisted bilayer MoS_2 are shown in Fig. 4a and b, respectively. The unit cell of the crystallographic superlattice with the 21.79° twist was the same as the moiré superlattice, as represented by the red parallelogram in Fig. 4b. In the reciprocal space, the large blue and orange hexagons represent the first Brillouin zones (BZ) of the top and bottom MoS_2 layers, respectively. Also, the solid green hexagons represent the Wigner–Seitz cells of the reciprocal lattices of the crystallographic superlattices. To easily understand the energy band structure, we obtained the effective band structure of the crystallographic superlattice of twisted bilayer MoS_2 by calculating the spectral weight $P_{\vec{K}m}(\vec{k}_i) = \sum_n \left|\left\langle \vec{K}m|\vec{k}_i n\right\rangle\right|^2$, where $P_{\vec{K}m}(\vec{k}_i)$ is the probability of finding a set of monolayer cell states $\left|\vec{k}_i n\right\rangle$ contributing to the superlattice states $\left|\vec{K}m\right\rangle$.[55] Theoretical effective band structure results along with high-symmetry lines are shown in Fig. 4c and d. It is seen that at the center region **0** with the interlayer distance $\Delta d_0 = d_0 - d_1 = 0.63$ nm (Fig. 4c), the valence band maximum (VBM) was located at the Γ point and the conduction band minimum (CBM) was located at the K point. This shows an indirect gap feature. However, at the off-center region **2′** with $\Delta d_{2'} = d_{2'} - d_1 = 0.95$ nm (Fig. 4d), both VBM and CBM were located at the K point, declaring a direct gap. The systematic theoretical results shown in Fig. 4c and d and Fig. S8† perfectly reproduced our experimental results of the indirect-to-direct band gap transition from the center region to the off-center region in the artificially prepared MoS_2 flowers. In a word, the expanded interlayer spacing further weakened the interlayer coupling to induce the PL intensity enhancement and the energy band structure transition from the indirect gap to the direct gap.

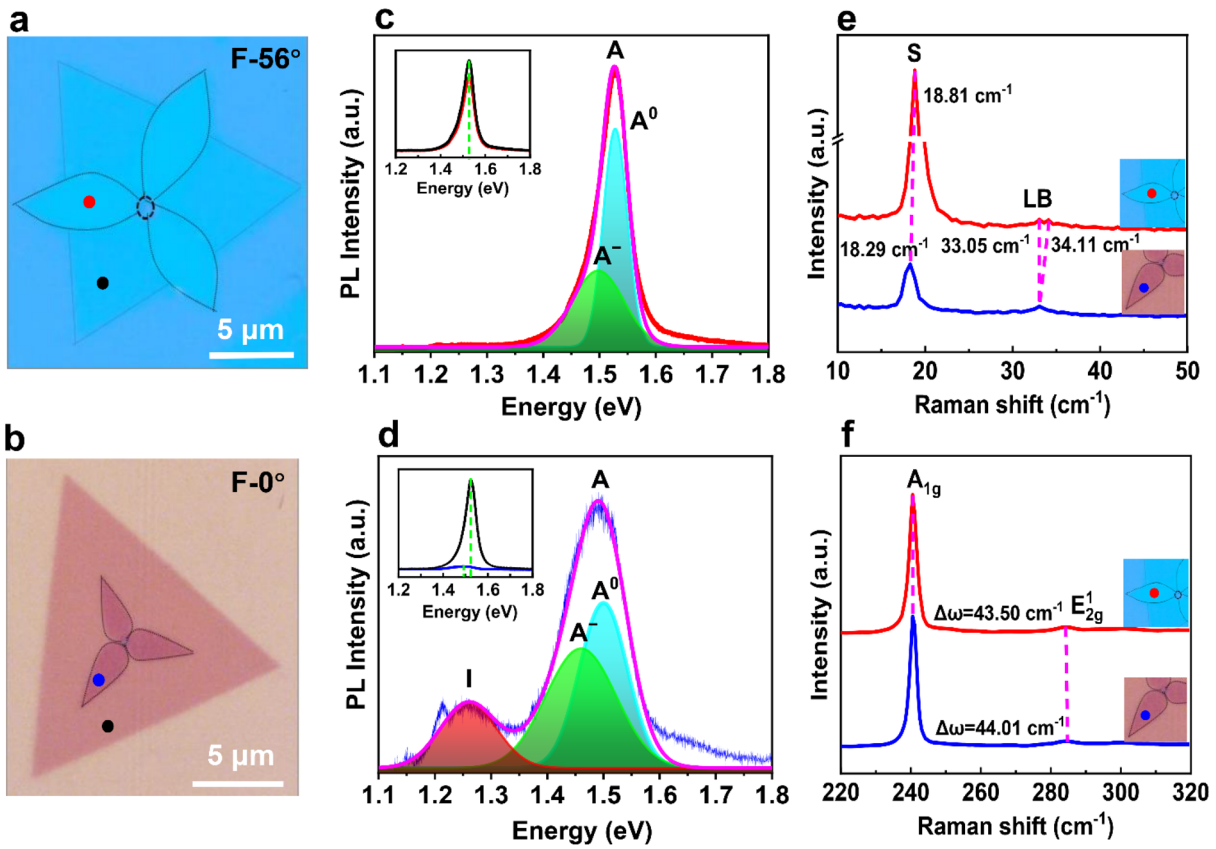

Fig. 5 Raman and PL measurements of tB-$MoSe_2$ flowers. (a and b) The OM image of the tB-$MoSe_2$ flower pattern with twist angles of 56 and 0°, respectively. The measured PL regions are highlighted by different colored dots in (a) and (b). (c and d) PL spectra of the 56°- and 0°-tB-$MoSe_2$ flower pattern with Gaussian fitting, respectively. The insets in the left upper corner of (c) and (d) show the comparable PL spectra obtained in the bilayer and monolayer regions of 56°-tB-$MoSe_2$ and 0°-tB-$MoSe_2$ flower patterns, respectively. (e and f) The LF and HF Raman spectra of respective 56°-tB-$MoSe_2$ and 0°-tB-$MoSe_2$ flower patterns.

Interestingly, similar results were observed in the tB-$MoSe_2$ flower pattern with a twist-angle of 56°. Fig. 5a and b shows OM images of the tB-$MoSe_2$ flower patterns with twist angles of 56° and 0°, respectively. Notably, the PL spectrum (the red curve shown in Fig. 5c) obtained in the top layer of the tB-$MoSe_2$ flower pattern showed almost the same character as that from the single-layer region (the black curve shown in Fig. 5c), as compared in the inset of the left corner shown in Fig. 5c. Here, the indirect gap disappeared in the red curve (the red curve) and the purple curve as shown in Fig. 5c. However, the PL result exhibited the typical feature of the bilayer $MoSe_2$ with an indirect gap at the energy of 1.261 eV. Fig. 5e shows the red and blue curve representations of LF Raman spectra corresponding to the 56°- and 0°-tB-$MoSe_2$ flower, respectively. Similarly, the LB mode in the 56°-tB-$MoSe_2$ flower sample split into two subpeaks. This is in accordance with the LF Raman results obtained for samples of 16°-, 21°-, 25°-, 30°-, 36°-, and 45°-tB-MoS_2 flowers. Meanwhile, from the HF Raman spectra of tB-$MoSe_2$ structures with twisted angles of 56° and 0° in Fig. 5f, we can find that the energy difference between A_{1g} and E^1_{2g} was enlarged to 44.01 cm^{-1} for the 56°-tB-$MoSe_2$ flower sample, compared to that (43.51 cm^{-1}) of sample 0°-tB-$MoSe_2$ flower. This suggests that the interlayer coupling was weakened in the 56°-tB-$MoSe_2$ flower sample. This result further verifies that the interlayer decoupling reliably helped the energy band structure change from the indirect gap to the direct one.

3. Conclusions

Artificially stacked bilayer MoS_2 flower patterns with versatile twisted angles (about 16°, 21°, 25°, 30°, 36°, and 45°) were controllably fabricated by the CVD approach. We found that the twisted bilayer MoS_2 (tB-MoS_2) flowers exhibit strong direct bandgap-like PL emission and overt monolayer-like optical properties in the region far from the flower center. In contrast, the 0° (60°) tB-MoS_2 flower patterns retained an indirect gap feature and weakened PL intensity. The above phenomenon on the direct bandgap-like behavior was reproducible in the tB-$MoSe_2$ flower with a twist angle of approximately 56°. The enlarged interlayer spacing induced the indirect-to-direct-gap transition and enhanced the PL intensity, resulting in interlayer decoupling and trion concentration reduction. This was verified by our DFT calculations on the effective mass of the electrons and holes and the energy band structures of the 21.79°-tB-MoS_2 moiré superstructure with different interlayer spacings. Our work provides a feasible method for the controllable preparation of artificially stacked structures to manipulate their energy band structures and the optical properties for their potential application in optical and optoelectronic nanodevices.

4. Methods

4.1 Fabrication of the twisted bilayer MoS_2 and $MoSe_2$ flower patterns

In our experiments, high-purity MoO_3 and S (Se) powder were used as precursors for the synthesis of MoS_2 and $MoSe_2$ in a CVD system with dual separately controlled temperature areas and Ar and H_2 were used as carrier gases. During the growth of tB-MoS_2 flower patterns, the S precursor (99.9%, 50 mg, Alfa Aesar) and the MoO_3 precursor (99.95%, 5 mg, Alfa Aesar) were placed on the low-temperature zone **I** and the high-temperature zone **II**, respectively. The distance between the S powder and the upstream MoO_3 powder was set at about 28 cm. Meanwhile, the 300 nm SiO_2/Si substrate was obliquely placed in a quartz boat with a tilted angle relative to the gas flow. The procedure of the growth of twisted bilayer MoS_2/$MoSe_2$ patterns was divided into four stages: (1) The rinsing stage: the CVD setup was rinsed with Ar gas at a flux of 1000 sccm for 10 min to remove air and other gases from the quartz tube, and the high-temperature zone **II** remains constant at 30 °C. (2) The heating stage: zone **II** was ramped from 30 °C to 800 °C for 20 min with an Ar flux of 100 sccm, and the low-temperature zone **I** was heated up from room temperature to 130 °C. (3) The growth stage: the low-temperature zone **I** and high-temperature zone **II** were held at 130 °C and 800 °C, respectively for 10 min under atmospheric pressure with an Ar flux of 200 sccm. (4) The cooling stage: dual temperature zones were gradually cooled down to room temperature with a gas flux 100 sccm.

As for the growth of tB-$MoSe_2$ flower patterns, the hydrogen (H_2) gas was introduced into the CVD setup. The carrier gases were hybrid gases of Ar and H_2, with a ratio of 5 to 1. Other experimental parameters are the same as those we used in the fabrication of MoS_2.

4.2 Characterization and measurement

LF and HF Raman spectra were measured at room temperature using a micro-Raman system (Horiba, LabRAM HR Evolution NANO) equipped with 1800 lines per mm gratings with a laser energy of 2.33 eV (532 nm). A 100× objective lens (numerical aperture = 0.90) was used to focus the laser beam to a spot of ~1 μm in diameter on the sample surface. PL spectra were recorded with a confocal Raman microscope (InVia, Renishaw U.K.) at room temperature with a 532 nm He–Cd laser as the excitation source. A 100 lines per mm grating was used in the PL measurements. AFM imaging was done under ambient conditions using a commercial atomic force microscope (NX10, park). A UV-vis-NIR spectrometer (Lambda 750, PerkinElmer) with a 532 nm laser as the excitation source.

4.3 DFT calculations of the energy band structure

DFT calculation of the energy band structure of the bilayer MoS_2 with a 21.79° twist and various interlayer spacings. Detailed calculation methods are listed in the ESI.†

Author contributions

J. Z. and J. C equally contributed to this work. R. F. D. and J. Z. conceived the present experiments. J. Z. prepared the MoS_2 and $MoSe_2$ bilayer samples on SiO_2/Si substrates. J. Z., X. T. L, S. D., Q. H. B, and Y. G. carried out the Raman spectrum measurements. J. Z., Z. H. Z., W. F. Z., and N. L. performed the PL measurements. J. Z., J. F. G., S. Y. L., S. M., and Z. H. C. carried out the AFM measurements. J. C. and Y. Y. carried out the theoretical calculations. R. F. D. and J. Z. analyzed the experimental data. R.F. D. completed writing this manuscript, discussed it with J. C. N. and L. H., and Y. Y. and J. C. provided help with theoretical analysis. All authors discussed the results and commented on the manuscript.

Conflicts of interest

There are no conflicts to declare.

Acknowledgements

R. F. D acknowledges the support from the National Natural Science Foundation of China (Grant No. 11974048, 11774192, 12074053, 62174179, 92265110, 12247125). This work was also supported by the open project of the State Key Laboratory of Low-Dimensional Quantum Physics, Tsinghua University. The authors thank Professor X. F. Liu and Professor J. P. Shi, National Center of Nanoscience and Technology, for their help in performing visible light adsorption spectroscopy.

References

1 L. A. Ponomarenko, R. V. Gorbachev, G. L. Yu, D. C. Elias, R. Jalil, A. A. Patel, A. Mishchenko, A. S. Mayorov, C. R. Woods, J. R. Wallbank, M. Mucha-Kruczynski, B. A. Piot, M. Potemski, I. V. Grigorieva, K. S. Novoselov, F. Guinea, V. I. Fal'ko and A. K. Geim, *Nature*, 2013, **497**, 594–597.

2 R. Bistritzer and A. H. MacDonald, *Proc. Natl. Acad. Sci. U. S. A.*, 2011, **108**, 12233–12237.

3 S. Manzeli, D. Ovchinnikov, D. Pasquier, O. V. Yazyev and A. Kis, *Nat. Rev. Mater.*, 2017, **2**, 17033.

4 G. L. Yu, R. V. Gorbachev, J. S. Tu, A. V. Kretinin, Y. Cao, R. Jalil, F. Withers, L. A. Ponomarenko, B. A. Piot, M. Potemski, D. C. Elias, X. Chen, K. Watanabe, T. Taniguchi, I. V. Grigorieva, K. S. Novoselov, V. I. Fal'ko, A. K. Geim and A. Mishchenko, *Nat. Phys.*, 2014, **10**, 525–529.

5 C. R. Dean, L. Wang, P. Maher, C. Forsythe, F. Ghahari, Y. Gao, J. Katoch, M. Ishigami, P. Moon, M. Koshino, T. Taniguchi, K. Watanabe, K. L. Shepard, J. Hone and P. Kim, *Nature*, 2013, **497**, 598–602.

6 B. Hunt, J. D. Sanchez-Yamagishi, A. F. Young, M. Yankowitz, B. J. LeRoy, K. Watanabe, T. Taniguchi, P. Moon, M. Koshino, P. Jarillo-Herrero and R. C. Ashoori, *Science*, 2013, **340**, 1427–1430.

7 Y. Cao, V. Fatemi, A. Demir, S. Fang, S. L. Tomarken, J. Y. Luo, J. D. Sanchez-Yamagishi, K. Watanabe, T. Taniguchi, E. Kaxiras, R. C. Ashoori and P. Jarillo-Herrero, *Nature*, 2018, **556**, 80–84.

8 Y. Cao, V. Fatemi, S. Fang, K. Watanabe, T. Taniguchi, E. Kaxiras and P. Jarillo-Herrero, *Nature*, 2018, **556**, 43–50.

9 M. L. Lin, Q. H. Tan, J. B. Wu, X. S. Chen, J. H. Wang, Y. H. Pan, X. Zhang, X. Cong, J. Zhang, W. Ji, P. A. Hu, K. H. Liu and P. H. Tan, *ACS Nano*, 2018, **12**, 8770–8780.

10 J. Quan, L. Linhart, M.-L. Lin, D. Lee, J. Zhu, C.-Y. Wang, W.-T. Hsu, J. Choi, J. Embley, C. Young, T. Taniguchi, K. Watanabe, C.-K. Shih, K. Lai, A. H. MacDonald, P.-H. Tan, F. Libisch and X. Li, *Nat. Mater.*, 2021, **20**, 1100–1105.

11 M. Liao, Z. Wei, L. Du, Q. Wang, J. Tang, H. Yu, F. Wu, J. Zhao, X. Xu, B. Han, K. Liu, P. Gao, T. Polcar, Z. Sun, D. Shi, R. Yang and G. Zhang, *Nat. Commun.*, 2020, **11**, 2153.

12 A. M. van der Zande, J. Kunstrnann, A. Chernikov, D. A. Chenet, Y. You, X. Zhang, P. Y. Huang, T. C. Berkelbach, L. Wang, F. Zhang, M. S. Hybertsen, D. A. Muller, D. R. Reichman, T. F. Heinz and J. C. Hone, *Nano Lett.*, 2014, **14**, 3869–3875.

13 I. Paradisanos, S. Shree, A. George, N. Leisgang, C. Robert, K. Watanabe, T. Taniguchi, R. J. Warburton, A. Turchanin, X. Marie, I. C. Gerber and B. Urbaszek, *Nat. Commun.*, 2020, **11**, 2391.

14 M. H. Naik and M. Jain, *Phys. Rev. Lett.*, 2018, **121**, 266401.

15 S. Sarkar, S. Mathew, S. Chintalapati, A. Rath, M. Panahandeh-Fard, S. Saha, S. Goswami, S. J. R. Tan, K. P. Loh, M. Scott and T. Venkatesan, *ACS Nano*, 2020, **14**, 16761–16769.

16 K. Liu, L. Zhang, T. Cao, C. Jin, D. Qiu, Q. Zhou, A. Zettl, P. Yang, S. G. Louie and F. Wang, *Nat. Commun.*, 2014, **5**, 4966.

17 P.-C. Yeh, W. Jin, N. Zaki, J. Kunstmann, D. Chenet, G. Arefe, J. T. Sadowski, J. I. Dadap, P. Sutter, J. Hone and R. M. Osgood Jr., *Nano Lett.*, 2016, **16**, 953–959.

18 H. J. Conley, B. Wang, J. I. Ziegler, R. F. Haglund Jr., S. T. Pantelides and K. I. Bolotin, *Nano Lett.*, 2013, **13**, 3626–3630.

19 A. Ramasubramaniam, D. Naveh and E. Towe, *Phys. Rev. B: Condens. Matter Mater. Phys.*, 2011, **84**, 205325.

20 S. B. Desai, G. Seol, J. S. Kang, H. Fang, C. Battaglia, R. Kapadia, J. W. Ager, J. Guo and A. Javey, *Nano Lett.*, 2014, **14**, 4592–4597.

21 Y. Y. Hui, X. Liu, W. Jie, N. Y. Chan, J. Hao, Y.-T. Hsu, L.-J. Li, W. Guo and S. P. Lau, *ACS Nano*, 2013, **7**, 7126–7131.

22 S. Deng, A. V. Sumant and V. Berry, *Nano Today*, 2018, **22**, 14–35.

23 Z. Li, Y. Lv, L. Ren, J. Li, L. Kong, Y. Zeng, Q. Tao, R. Wu, H. Ma, B. Zhao, D. Wang, W. Dang, K. Chen, L. Liao, X. Duan, X. Duan and Y. Liu, *Nat. Commun.*, 2020, **11**, 1151.
24 S. Tongay, J. Zhou, C. Ataca, K. Lo, T. S. Matthews, J. Li, J. C. Grossman and J. Wu, *Nano Lett.*, 2012, **12**, 5576–5580.
25 R. Dhall, M. R. Neupane, D. Wickramaratne, M. Mecklenburg, Z. Li, C. Moore, R. K. Lake and S. Cronin, *Adv. Mater.*, 2015, **27**, 1573–1578.
26 B. Wang, S. Yang, J. Chen, C. Mann, A. Bushmaker and S. B. Cronin, *Appl. Phys. Lett.*, 2017, **111**, 131101.
27 W. Zhou, X. Zou, S. Najmaei, Z. Liu, Y. Shi, J. Kong, J. Lou, P. M. Ajayan, B. I. Yakobson and J.-C. Idrobo, *Nano Lett.*, 2013, **13**, 2615–2622.
28 H. Nan, Z. Wang, W. Wang, Z. Liang, Y. Lu, Q. Chen, D. He, P. Tan, F. Miao, X. Wang, J. Wang and Z. Ni, *ACS Nano*, 2014, **8**, 5738–5745.
29 R. Sebait, C. Biswas, B. Song, C. Seo and Y. H. Lee, *ACS Nano*, 2021, **15**, 2849–2857.
30 (*a*) S. Huang, L. Liang, X. Ling, A. A. Puretzky, D. B. Geohegan, B. G. Sumpter, J. Kong, V. Meunier and M. S. Dresselhaus, *Nano Lett.*, 2016, **16**, 1435–1444; (*b*) Y. Z. Zhao, C. Y. Zhang, D. D. Kohler, J. M. Scheeler, J. C. Wright, P. M. Voyles and S. Jin, *Science*, 2020, **370**, 442–445; (*c*) X. Y. Li, S. P. Zhang, S. Chen, X. L. Zhang, J. F. Gao, Y.-W. Zhang, J. J. Zhao, X. Shen, R. C. Yu, Y. Yang, L. He, J. C. Nie, C. M. Xiong and R. F. Dou, *ACS Appl. Mater. Interfaces*, 2019, **11**, 42751–42759.
31 L. Sun, Z. Wang, Y. Wang, L. Zhao, Y. Li, B. Chen, S. Huang, S. Zhang, W. Wang, D. Pei, H. Fang, S. Zhong, H. Liu, J. Zhang, L. Tong, Y. Chen, Z. Li, M. H. Rummeli, K. S. Novoselov, H. Peng, L. Lin and Z. Liu, *Nat. Commun.*, 2021, **12**, 2391–2391.
32 A general method and the growth mechanism for the direct preparation of twisted bilayer MoS_2 on SiO_2/Si by chemical vapour deposition.
33 R. Dhall, M. R. Neupane, D. Wickramaratne, M. Mecklenburg, Z. Li, C. Moore, R. K. Lake and S. Cronin, *Adv. Mater.*, 2015, **27**, 1573–1578.
34 S. Huang, X. Ling, L. Liang, J. Kong, H. Terrones, V. Meunier and M. S. Dresselhaus, *Nano Lett.*, 2014, **14**, 5500–5508.
35 L. Liang, J. Zhang, B. G. Sumpter, Q.-H. Tan, P.-H. Tan and V. Meunier, *ACS Nano*, 2017, **11**, 11777–11802.
36 X. Lu, M. I. B. Utama, J. Lin, X. Luo, Y. Zhao, J. Zhang, S. T. Pantelides, W. Zhou, S. Y. Quek and Q. Xiong, *Adv. Mater.*, 2015, **27**, 4502–4508.
37 A. A. Puretzky, L. Liang, X. Li, K. Xiao, K. Wang, M. Mahjouri-Samani, L. Basile, J. C. Idrobo, B. G. Sumpter, V. Meunier and D. B. Geohegan, *ACS Nano*, 2015, **9**, 6333–6342.
38 X. Luo, X. Lu, C. Cong, T. Yu, Q. Xiong and S. Y. Quek, *Sci. Rep.*, 2015, **5**, 14565.
39 K. Kim, J.-U. Lee, D. Nam and H. Cheong, *ACS Nano*, 2016, **10**, 8113–8120.
40 X. Lu, M. I. B. Utama, J. Lin, X. Gong, J. Zhang, Y. Zhao, S. T. Pantelides, J. Wang, Z. Dong, Z. Liu, W. Zhou and Q. Xiong, *Nano Lett.*, 2014, **14**, 2419–2425.
41 J.-U. Lee, S. Woo, J. Park, H. C. Park, Y.-W. Son and H. Cheong, *Nat. Commun.*, 2017, **8**, 1370.
42 X. Du, Y. Lee, Y. Zhang, T. Yu, K. Kim and N. Liu, *ACS Appl. Mater. Interfaces*, 2021, **13**, 22819–22827.
43 K. Suenaga, H. G. Ji, Y.-C. Lin, T. Vincent, M. Maruyama, A. S. Aji, Y. Shiratsuchi, D. Ding, K. Kawahara, S. Okada, V. Panchal, O. Kazakova, H. Hibino, K. Suenaga and H. Ago, *ACS Nano*, 2018, **12**, 10032–10044.
44 Z. Ma, S. Wang, Q. Deng, Z. Hou, X. Zhou, X. Li, F. Cui, H. Si, T. Zhai and H. Xu, *Small*, 2020, **16**, 2000596.
45 W. Zhang, Z. Zhao, Y. Yang, Y. Zhang, H. Hao, L. Li, W. Xu, B. Peng, R. Long and N. Liu, *ACS Appl. Mater. Interfaces*, 2021, **13**, 40922–40931.
46 C. Lee, H. Yan, L. E. Brus, T. F. Heinz, J. Hone and S. Ryu, *ACS Nano*, 2010, **4**, 2695–2700.
47 P. H. Tan, W. P. Han, W. J. Zhao, Z. H. Wu, K. Chang, H. Wang, Y. F. Wang, N. Bonini, N. Marzari, N. Pugno, G. Savini, A. Lombardo and A. C. Ferrari, *Nat. Mater.*, 2012, **11**, 294–300.
48 Y. Wang, C. Cong, C. Qiu and T. Yu, *Small*, 2013, **9**, 2857–2861.
49 D. Lloyd, X. Liu, J. W. Christopher, L. Cantley, A. Wadehra, B. L. Kim, B. B. Goldberg, A. K. Swan and J. S. Bunch, *Nano Lett.*, 2016, **16**, 5836–5841.
50 B. Liu, Q. Liao, X. Zhang, J. Du, Y. Ou, J. Xiao, Z. Kang, Z. Zhang and Y. Zhang, *ACS Nano*, 2019, **13**, 9057–9066.
51 Z. Liu, M. Amani, S. Najmaei, Q. Xu, X. Zou, W. Zhou, T. Yu, C. Qiu, A. G. Birdwell, F. J. Crowne, R. Vajtai, B. I. Yakobson, Z. Xia, M. Dubey, P. M. Ajayan and J. Lou, *Nat. Commun.*, 2014, **5**, 5246.
52 T. Li and G. Galli, *J. Phys. Chem. C*, 2007, **111**, 16192–16196.
53 S. Guo, Y. Zhang, S. Tang, B. Wang, Y. Wang, Y. Song, X. Xin, Y. Zhang and X. Li, *J. Alloys Compd.*, 2021, **864**, 158581.
54 J. S. Ross, S. F. Wu, H. Y. Yu, N. J. Ghimire, A. M. Jones, G. Aivazian, J. Q. Yan, D. G. Mandrus, D. Xiao, W. Yao and X. D. Xu, *Nat. Commun.*, 2013, **4**, 1474.
55 V. Popescu and A. Zunger, *Phys. Rev. B: Condens. Matter Mater. Phys.*, 2012, **85**, 085201.